RSC Advances

PAPER

View Article Online
View Journal | View Issue

Cite this: *RSC Adv.*, 2026, **16**, 20609

One-pot mechanochemical access to quinoline-linked covalent organic frameworks

Yizhou Zhan, †*[ac] Yuxuan Yang,†[a] Wei Zhao,[a] Xi Wang,[a] Jiarong Qiu,[a] Zhaonan Tang,[d] Jiao He,[e] Chenglong Deng,[e] Heshen Xiao,[f] Yiying Pang*[bc] and Xiaoji Wang*[bc]

Quinoline-linked COFs are formed by transforming reversible imine bonds into irreversible, π-extended quinoline linkages, thereby enhancing framework robustness and structural stability. Most reported syntheses, however, still rely on solvothermal methods that require high temperatures, multi-day reactions, and hazardous solvents. While mechanochemical synthesis has emerged as a solid-state and scalable alternative for COF construction, existing studies have predominantly focused on reversible linkages, such as imine and β-ketoenamine bonds, leaving the direct formation of irreversible quinoline-linked frameworks largely unexplored. Herein, we report a one-pot mechanochemical Povarov cascade that enables the *in situ* formation of imine-linked intermediates followed by their conversion into quinoline-linked COFs within a single vessel under open-air, room-temperature conditions. The reaction is completed within ~3.5 h, affording eleven structurally diverse quinoline-linked COFs with high crystallinity and well-defined porosity, while requiring only trace amounts of liquid additives and supporting gram-scale synthesis. Comprehensive structural characterization confirms that the mechanochemically synthesized quinoline-linked COFs exhibit structural features comparable to those of solvothermal analogues. This work demonstrates an efficient solid-state route to irreversible linkage construction in COFs and broadens the scope of mechanochemical strategies for the synthesis of robust porous frameworks.

Received 11th February 2026
Accepted 13th April 2026

DOI: 10.1039/d6ra01241h

rsc.li/rsc-advances

1 Introduction

Covalent organic frameworks (COFs) are crystalline porous polymers assembled from light elements through strong covalent bonds, featuring permanent porosity, long-range order, and modular structural tunability, which enable broad applications.[1–4] The formation of highly crystalline COFs typically relies on reversible dynamic covalent chemistry (*e.g.*, imine, boroxine, and boronate-ester formation) under thermodynamic control, most commonly achieved *via* solvothermal synthesis at elevated temperatures in sealed vessels.[5] However, the trade-off between reversible linkages enabling crystallinity and their inherent chemical instability remains a central challenge in COF chemistry, motivating the development of more stable framework architectures.[6]

To address this challenge, irreversible linkages such as dioxin, ester, vinylene, triazine, and sp^2 carbon linkages have been introduced to improve COF stability.[7–11] However, their limited reversibility often compromises error correction and crystallinity control. An alternative strategy involves post-assembly linkage transformation through one-pot reactions (OPR) or post-synthetic modifications (PSM).[12] In imine-linked COFs, such transformations convert reversible –C=N– bonds into rigid, conjugated N-heterocycles (*e.g.*, benzimidazole, phenazine, or quinoline), thereby combining enhanced chemical stability with extended π-conjugation.[6] Among these, quinoline linkages are particularly attractive due to their chemical robustness and extended electronic delocalization.[13,14] Despite growing interest, the synthesis of quinoline-linked COFs remains largely confined to solvothermal routes, including the Povarov reaction,[14–19] Doebner reaction,[20] and related approaches.[21] These methods typically require high temperatures, prolonged reaction times (several days), and inert

[a]*School of Materials Science and Engineering, Dongguan University of Technology, Dongguan, 523808, P.R. China. E-mail: zhanyizhou@dgut.edu.cn*

[b]*School of Chemical Engineering and Energy Technology, Dongguan University of Technology, Dongguan, 523808, P.R. China. E-mail: wangxj@dgut.edu.cn; pangyiying@dgut.edu.cn*

[c]*Songshan Lake Innovation Center of Medicine and Engineering, Dongguan University of Technology, Dongguan, 523808, P.R. China*

[d]*School of Life and Health Technology, Dongguan University of Technology, Dongguan 523808, P.R. China*

[e]*College of Chemistry and Environmental Engineering, Key Laboratory of Green Catalysis of Higher Education Institutes of Sichuan, Sichuan University of Science and Engineering, Zigong 643000, P. R. China*

[f]*Analytical and Testing Center, Dongguan University of Technology, Dongguan, 523808, P.R. China*

† These authors contributed equally to this work.

or sealed conditions, which severely limit scalability and sustainability.

Mechanochemistry has recently emerged as a solvent-minimized and scalable solid-state platform for materials synthesis,[22–24] with successful applications in nanoparticles,[25] pharmaceuticals,[26] cocrystals,[27] polymers,[28] metal–organic frameworks (MOFs),[29] and COFs.[30–35] Within COFs research, mechanochemistry has enabled the synthesis of β-ketoenamine-linked COFs,[30] imine-linked COFs,[31,32] yet its application has so far been largely limited to simple, reversible linkages. Only very recently has mechanochemistry been extended to more complex linkages, including boroxine[33] and covalent triazine linkages.[34] Very recently, during the submission of this work, related mechanochemical multicomponent strategies for COF synthesis were accepted for publication.[36] This study was developed independently and in parallel, providing a complementary mechanochemical approach to the construction of quinoline-linked COFs.

Herein, we report a mechanochemical Povarov cascade for the synthesis of quinoline-linked COFs. In this solid-state process, crystalline imine-linked COFs are assembled *in situ* and subsequently transformed within the same vessel *via* aza-Diels–Alder cycloaddition followed by oxidative aromatization, yielding quinoline-linked COFs with irreversible, π-extended linkages. Compared with solvothermal routes, this strategy shortens reaction times from days to hours, drastically reduces solvent consumption, and enables gram-scale synthesis while preserving high crystallinity. Moreover, the method exhibits broad monomer compatibility, affording structurally diverse quinoline-linked COFs from various building blocks. This work establishes a general solid-state pathway for constructing chemically robust quinoline-linked COFs and expands mechanochemistry beyond reversible framework synthesis.

2 Experiments

2.1. Chemicals

All of the reagents are commercially accessible and can be used immediately.

2.2. Characterization

^{1}H-NMR and ^{13}C-NMR spectra were recorded on a Bruker Avance Neo 400 MHz spectrometer in the given solvent. Data are reported in the following order: chemical shift (δ) in ppm; multiplicities (br for broadened singlet, s for singlet, d for doublet, t for triplet, m for multiplet); coupling constants (J) in Hertz (Hz); number of protons. Solid-state ^{13}C cross-polarization magic-angle spinning (^{13}C CP/MAS NMR) spectra were recorded on a Bruker AVANCE NEO 600 spectrometer (Germany) operating at a resonance frequency of 600 MHz. The scanning electron microscope (SEM) measurement was conducted by VeriosG4UC. The Fourier transform infrared spectroscopy (FT-IR) analyses of the samples were performed on a PerkinElmer FRONTIER spectrometer. Powder X-ray diffraction (PXRD) patterns were recorded on a Bruker D8 ADVANCE instrument with Cu-K$_\alpha$ radiation ($\lambda = 1.5406$ Å) over a 2θ range of 1.5–30°. N_2 adsorption/desorption isotherms were measured at 77 K on a Micromeritics ASAP 2460 analyzer, with a degassing temperature of 120 °C for 8 h before the measurement. The specific surface areas were calculated by using Brunauer–Emmett–Teller (BET) calculations and the pore size distributions were obtained by the non-localized density functional theory (NLDFT) model. Thermogravimetric analyses (TGA) were carried out on a NETZSCH STA 449 F5 Jupiter analytical instrument under a N_2 atmosphere, with the temperature increasing from room-temperature to 1000 °C at a heating rate of 10 °C min^{-1}. X-ray photoelectron spectroscopy (XPS) using a Thermo Fisher K-Alpha instrument was employed to investigate the chemical elements and components of the materials.

2.3. Synthesis of model compound

Into a 10 mL stainless steel milling jar, amine monomer (0.07 mmol, 1 equiv.), aldehyde monomer (0.07 mmol, 1 equiv.), mesitylene (40 μL), and glacial acetic acid (20 μL) were added along with four 4 mm steel balls. The reaction mixture was milled in a Retsch MM 400 Mixer Mill at 30 Hz for 1.5 h at room-temperature. After that, aryl alkyne monomer (0.21 mmol, 3 equiv.), $BF_3{\cdot}OEt_2$ (0.084 mmol, 1.2 equiv.), and chloranil (0.084 mmol, 1.2 equiv.) were added to the stainless steel milling jar, and the mixture was further milled at 30 Hz for 2 h at room-temperature. After completion of the reaction, the product was transferred to an eggplant-shaped flask using dichloromethane and dried on a rotary evaporator. The concentrated residue was purified by silica gel flash column chromatography using petroleum ether (PE)/ethyl acetate (EA) as the eluent.

2.4. Mechanochemical synthesis of imine-linked COFs

Into a 10 mL stainless steel milling jar, amine monomer (0.28 mmol, 1 equiv.), aldehyde monomer (0.28 mmol, 1 equiv.), mesitylene (160 μL), and glacial acetic acid (80 μL) were added along with four 4 mm steel balls. The reaction mixture was milled in a Retsch MM 400 Mixer Mill at 30 Hz for 1.5 h at room-temperature. The solid in the stainless steel milling jar was removed, immersed in *N*,*N*-dimethylformamide (DMF) in a small glass vial, and ultrasonically dispersed for 2 min. The sample was transferred to a suction funnel, washed first with DMF and then with acetone until the filtrate was colorless. It was transferred to filter paper and purified by Soxhlet extraction (using tetrahydrofuran) for 24 h. The wet powder was dried at 110 °C under a high vacuum overnight.

2.5. Mechanochemical synthesis of quinoline-linked COFs

Into a 10 mL stainless steel milling jar, amine monomer (0.28 mmol, 1 equiv.), aldehyde monomer (0.28 mmol, 1 equiv.), mesitylene (160 μL), and glacial acetic acid (80 μL) were added along with four 4 mm steel balls. The reaction mixture was milled in a Retsch MM 400 Mixer Mill at 30 Hz for 1.5 h at room-temperature. After that, aryl alkyne monomer (0.84 mmol, 3 equiv.), $BF_3{\cdot}OEt_2$ (0.34 mmol, 1.2 equiv.), and chloranil (0.34 mmol, 1.2 equiv.) were added to the stainless steel milling jar, and the mixture was further milled at 30 Hz for 2 h at room-

temperature. The solid in the stainless steel milling jar was removed, immersed in DMF in a small glass vial, and ultrasonically dispersed for 2 min. The sample was transferred to a suction funnel, washed first with DMF and then with acetone until the filtrate was colorless, and then placed on filter paper. Residual $BF_3 \cdot OEt_2$ was removed by Soxhlet extraction with tetrahydrofuran (THF) for 24 h, followed by drying under high vacuum at 110 °C for 12 h.

2.6. Chemical stability test

The as-synthesized TFPB-TPB-COF and TFPB-TPB-COF-H were separately placed in glass vials containing 5 mL of respective test media: both COFs were exposed to 12 M HCl, 12 M NaOH, 5 M $KMnO_4$ (in acetonitrile), and 5 M $NaBH_4$ (in THF); additionally, TFPB-TPB-COF-H was further tested in DMSO, ethanol, acetonitrile, and H_2O. A magnetic stir bar was added to each vial, and all mixtures were stirred for 72 h. Subsequently, the samples were transferred to a Buchner funnel, washed sequentially with distilled water and THF until the filtrate became colorless. The washed samples were dried overnight at 110 °C under high vacuum, followed by powder X-ray diffraction (PXRD) measurements.

3 Results and discussion

3.1. Mechanochemical Povarov cascade for COF construction

To validate the feasibility of the mechanochemical Povarov cascade, a solid-state small-molecule model reaction was first examined (Scheme 1a). Solid aniline (1a) and aldehyde (1b) were chosen to mimic the solid–solid environment of COF synthesis. Under liquid-assisted grinding, rapid imine formation occurred, giving the corresponding intermediate (1c) with 97% conversion, as confirmed by ^{1}H NMR spectroscopy. Without isolating the imine intermediate, subsequent addition of phenylacetylene and $BF_3 \cdot OEt_2$ enabled a one-pot cascade involving aza-Diels–Alder cycloaddition and oxidative aromatization, yielding the quinoline product (1d) in 82% isolated yield under ambient conditions (Fig. S1–S4). These results demonstrate that the multistep Povarov cascade is fully compatible with solid-state mechanochemical operation.

Encouraged by the model reaction, this strategy was directly extended to the construction of covalent organic frameworks (Scheme 1b). Under identical milling conditions, crystalline imine-linked COFs formed initially and could be isolated on demand, while prolonged milling in the same vessel induced *in situ* aza-Diels–Alder cycloaddition and oxidative aromatization to afford quinoline-linked COFs without intermediate isolation. Importantly, this cascade proceeds through controlled reaction progression under continuous milling, without interruption or isolation of discrete intermediates. This one-pot, stepwise linkage evolution enables controllable access to either reversible imine- or irreversible quinoline-linked frameworks from a single synthetic platform, demonstrating that framework connectivity can be regulated by reaction progression under mechanochemical conditions. The generality of this strategy was demonstrated by four structurally distinct COF systems (TFPB-TPB, TFPB-TTA, TTB-TPB, and TTB-TTA) and their quinoline derivatives. In particular, the TFPB-TPB-COF-R series tolerated diverse terminal substituents (-H, -F, -Cl, -OMe, and -CN), highlighting the broad functional-group compatibility of the mechanochemical cascade. Scalability was further confirmed by a 40-fold synthesis of TFPB-TPB-COF-H, delivering 1.37 g of highly crystalline material within 3.5 h (Fig. S14), underscoring the robustness and practical viability of this solid-state approach.

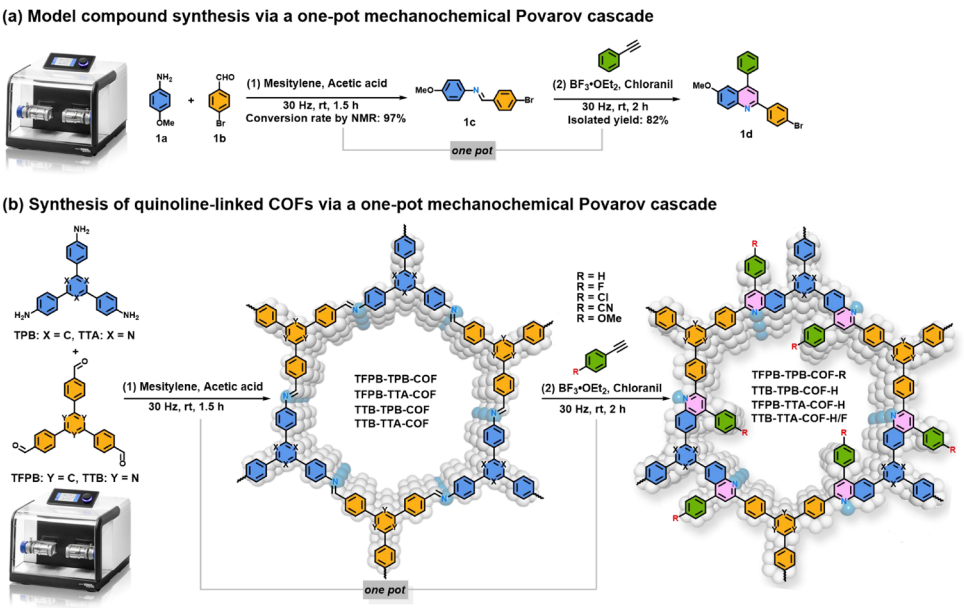

Scheme 1 Synthetic routes for (a) model compound, and (b) quinoline-linked COFs *via* a one-pot mechanochemical Povarov cascade.

3.2. Spectroscopic verification of imine-to-quinoline linkage transformation

The imine-to-quinoline linkage transformation was verified by complementary spectroscopic techniques, including Fourier transform infrared (FT-IR) spectroscopy, magic-angle-spinning (CP-MAS) ^{13}C NMR spectroscopy, and X-ray photoelectron spectroscopy (XPS). Imine-linked COFs exhibited characteristic –C═N– stretching bands at 1596–1626 cm^{-1}, consistent with Schiff-base formation.[37,38] After mechanochemical conversion, new bands appeared at 1583–1607 cm^{-1}, assignable to quinoline –C═N– vibrations,[39] accompanied by pronounced attenuation of the original imine signals (Fig. 1a and S23). Residual imine bands were weak, indicating effective but incomplete linkage conversion under solid-state conditions, while the preserved diffraction features confirm retention of long-range crystallinity. Notably, the peak at 1626 cm^{-1} largely diminished in the derivative of TTB-TPB-COF, providing direct evidence for a high conversion of imine bonds to quinoline moieties (Fig. S23d). Functional-group incorporation was further confirmed by diagnostic vibrations. TFPB-TPB-COF-CN displayed a distinct absorption at 2209 cm^{-1}, indicating the incorporation of the phenylacetylene-derived nitrile into the framework (Fig. 1a, red). Solid-state CP-MAS ^{13}C NMR spectroscopy further supported linkage evolution, with the imine –C═N– resonance shifting from δ 157 ppm (TFPB-TPB-COF) to δ 153 ppm (TFPB-TPB-COF-H) after quinoline formation, consistent with reported quinoline carbons.[17] XPS analysis further substantiated the linkage evolution and functionalization. The N 1s peak assignments were made by comparison with previously reported XPS data for structurally related quinoline-linked COFs and related nitrogen-containing frameworks.[14,15,19,40] Imine-linked TFPB-TPB-COF showed a single N 1s component at ~398.8 eV, assigned to imine nitrogen (Fig. 1c). After conversion, an additional N 1s signal at ~399.5 eV emerged, characteristic of pyridinic nitrogen in quinoline linkages (Fig. 1d and S24).[18] Element-specific XPS signals (F 1s, Cl 2p, and O 1s) confirmed the successful incorporation of terminal substituents (Fig. S24 and S25). Quantitative analysis of the N 1s peak-area ratios indicated apparent linkage-conversion degrees of 41% (R = H), 49% (R = F), 38% (R = Cl), 60% (R = OMe), and 17% (R = CN) for the respective quinoline-linked COFs, which were comparable to values reported for solvothermal syntheses.[39] Taken together, the consistent spectroscopic signatures across FT-IR, solid-state NMR, and XPS unambiguously confirm the mechanochemical imine-to-quinoline transformation while preserving framework integrity.

3.3. Structural integrity, porosity, and stability

Powder X-ray diffraction (PXRD) confirmed that high crystallinity and long-range order were preserved throughout the mechanochemical transformation. As shown in Fig. 2a and S26, the PXRD patterns of TFPB-TPB-COF displayed five well-defined diffraction peaks at 2θ = 4.00°, 6.95°, 8.09°, 10.66°, and 24.17°, which were indexed to the (100), (110), (200), (120), and (001) planes, respectively.[37–39] After conversion, the quinoline-linked derivatives displayed nearly identical diffraction profiles, with only a slight shift of the (100) reflection and preserved lattice indexing.[13] Importantly, gram-scale products and additional quinoline-linked COFs (TFPB-TTA-COF-H, TTB-TPB-COF-H, and TTB-TTA-COF-H) displayed similarly well-resolved PXRD patterns (Fig. S26 and S27), confirming the robustness and generality of this approach.

The permanent porosity and textural properties of the mechanochemically synthesized COFs were investigated by N_2 adsorption–desorption measurements at 77 K. The Brunauer–Emmett–Teller (BET) surface area of TFPB-TPB-COF was 568.7 m^2 g^{-1}, with a pore diameter of 1.86 nm (Fig. 2b). The quinoline-linked derivatives (TFPB-TPB-COF-H, -F, -Cl, -OMe,

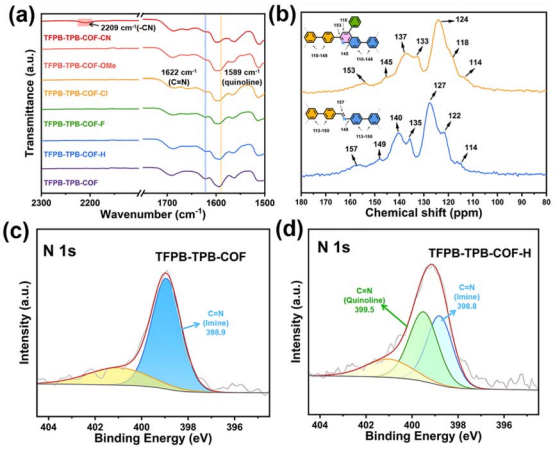

Fig. 1 FT-IR spectra of (a) TFPB-TPB-COF before and after imine-to-quinoline conversion. (b) Solid-state ^{13}C NMR spectra of TFPB-TPB-COF (blue line) and TFPB-TPB-COF-H (yellow line). High resolution N 1s XPS spectra of (c) TFPB-TPB-COF, (d) TFPB-TPB-COF-H. Note: the N 1s peak centered at 401 eV is assigned to the unreacted –NH_2 at the defective edges of COF (yellow area).

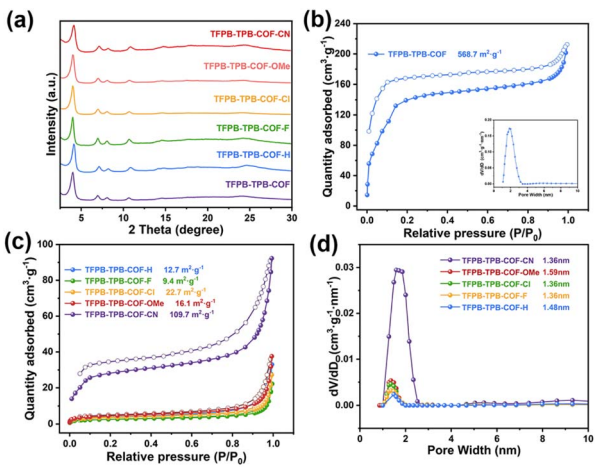

Fig. 2 (a) PXRD patterns of TFPB-TPB-COF before and after imine-to-quinoline conversion. N_2 adsorption–desorption isotherms and corresponding pore-size distributions of (b) TFPB-TPB-COF, after imine-to-quinoline conversion of (c) and (d) TFPB-TPB-COF-R.

-CN) showed substantially reduced surface areas (9.4–109.7 $m^2 g^{-1}$) after linkage transformation (Fig. 2c and d).[39,41] This decrease is attributed to the incorporation of bulky phenylacetylene groups during the aza-Diels–Alder/oxidative-aromatization cascade, which partially occupied the pore volume and increased framework density.[13,15,18] Control experiments, including repeated BET measurements and solvothermal synthesis of TFPB-TPB-COF-F, revealed only a modest surface-area increase (from 9.4 to 42.4 $m^2 g^{-1}$), indicating that the reduced porosity primarily originates from the intrinsic packing characteristics of this quinoline-linked skeleton rather than the synthetic method (Fig. S28). In contrast, the nitrogen-rich TTB-TTA-COF series exhibited much higher surface areas (up to 1710 $m^2 g^{-1}$), and its quinoline-linked derivatives retained substantial porosity (1380–1539 $m^2 g^{-1}$) (Fig. S29 and S30). These results demonstrate that porosity in quinoline-linked COFs is governed by linkage topology and molecular design, offering a handle for tuning framework architecture while preserving crystallinity.

Field-emission scanning electron microscopy (FESEM) revealed that the particulate morphology was largely retained after linkage conversion, while quinoline-linked COFs exhibited denser, rougher aggregates with substituent-dependent textures, reflecting steric and polarity effects on framework packing (Fig. S31).

The enhanced robustness of quinoline-linked COFs was further demonstrated by chemical and thermal stability tests using TFPB-TPB-COF and its quinoline-linked analogue as representatives. Unlike the imine-linked analogue, quinoline-linked COFs retained crystallinity after exposure to strong acids, bases, redox agents, and common solvents, while also exhibiting thermal stability above 500 °C (Fig. 3). The enhanced chemical and thermal stability of the quinoline-linked COF is attributed to the irreversible quinoline linkage, highlighting the robustness imparted by the mechanochemical transformation.[18,32,42]

To demonstrate the generality of the mechanochemical strategy, two additional COF systems with distinct topologies were synthesized under identical conditions (Scheme 2). In both cases, the one-pot reaction was completed within ~3.5 h, affording quinoline-linked COFs with high crystallinity. Linkage conversion, framework integrity, and thermal stability were confirmed by complementary spectroscopy and sorption analyses (Fig. S32–S38). Notably, both systems were successfully scaled to gram quantities without loss of crystallinity (Fig. S27), highlighting the robustness, scalability, and broad applicability of this mechanochemical approach.

3.4. Comparison with conventional solvothermal synthesis

To contextualize the mechanochemical strategy, representative quinoline-linked COFs synthesized herein were compared with solvothermal analogues reported in the literature (Table S1).[43,44] Conventional solvothermal routes typically require elevated temperatures (120 °C), prolonged reaction times (72–144 h), sealed vessels, and inert or vacuum atmospheres, often employing high-boiling organic solvents such as *o*-dichlorobenzene, mesitylene, or dioxane. In contrast, the one-pot mechanochemical Povarov cascade proceeds at room temperature under open-air conditions using only trace liquid additives, with η value (the ratio of liquid additive volume to product mass, μL mg^{-1}) ranged from 0.71 to 1.37, well within the liquid-assisted grinding (LAG) regime ($0 < \eta \lesssim$ 1–2 μL mg^{-1}), confirming efficient activation with minimal solvent input.[14,17,32] Notably, high isolated yields were achieved (*e.g.*, 90.5% for TTB-TTA-COF-H and 87.6% for TTB-TTA-COF-F), comparable to or exceeding solvothermal routes. Several mechanochemically synthesized COFs retained porosity comparable to solvothermal products, exemplified by TTB-TTA-COF-H (1538.7 $m^2 g^{-1}$) and TTB-TTA-COF-F (1380.1 $m^2 g^{-1}$). Lower surface areas observed for DMTP-TPB-COF-H (179 $m^2 g^{-1}$) are attributed to rapid gelation and partial pore blocking, rather than loss of

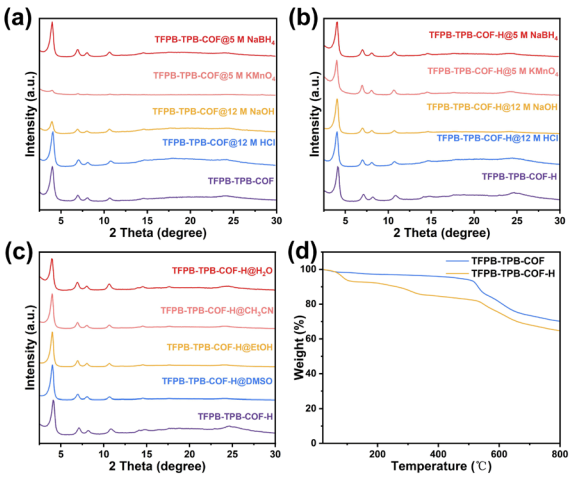

Fig. 3 PXRD patterns of (a) TFPB-TPB-COF and (b) TFPB-TPB-COF-H after soaking in strong acid (12 M HCl), strong base (12 M NaOH), strong oxidant (5 M $KMnO_4$ in acetonitrile), and reducing agent (5 M $NaBH_4$ in THF) for 72 h. PXRD patterns of (c) TFPB-TPB-COF-H after soaking in different organic solvents or water for 72 h. (d) TGA curves of TFPB-TPB-COF-H under an N_2 atmosphere.

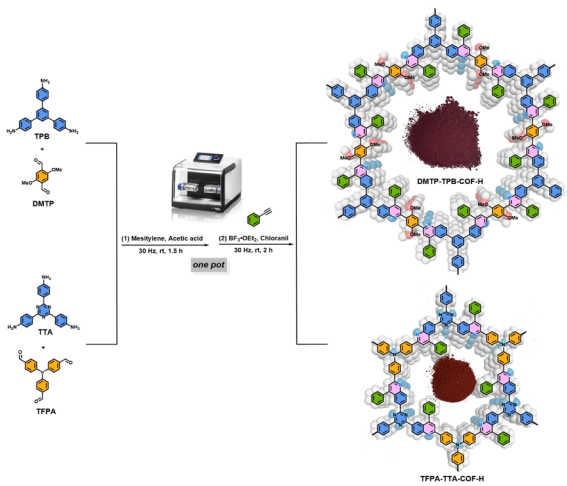

Scheme 2 Synthesis of quinoline-linked DMTP-TPB-COF-H and TFPA-TTA-COF-H *via* a one-pot mechanochemical Povarov cascade.

crystallinity.[23] PXRD confirmed preserved long-range order across all systems. Overall, this comparison highlights the mechanochemical Povarov cascade as a milder, faster, and more sustainable route to quinoline-linked COFs with structural fidelity comparable to solvothermal synthesis.

4 Conclusions

In conclusion, we demonstrate a one-pot mechanochemical Povarov cascade as a rapid and general solid-state strategy for constructing quinoline-linked COFs under ambient conditions. By integrating imine formation, cycloaddition, and oxidative aromatization within a single milling process, this approach circumvents prolonged solvothermal treatments while enabling irreversible linkage formation with preserved crystallinity. The method is broadly applicable, scalable to the gram level, and operates with minimal solvent input, expanding mechanochemical COF synthesis beyond reversible frameworks. These results establish solid-state cascade chemistry as a viable platform for accessing robust COFs and may stimulate further exploration of irreversible linkages in crystalline porous materials.

Author contributions

Yizhou Zhan: conceptualization, supervision, writing – review & editing; Yiying Pang: supervision, writing – review & editing; Yuxuan Yang: investigation, data curation, writing – original draft; Xi Wang: investigation, data curation; Jiarong Qiu: investigation, data curation; Wei Zhao: investigation, data curation; Zhaonan Tang: investigation, data curation; Jiao He: writing – review & editing, formal analysis; Chenglong Deng: writing – review & editing, formal analysis; Heshen Xiao: formal analysis; Xiaoji Wang: project administration, funding acquisition, resources. All authors discussed the results and approved the final manuscript.

Conflicts of interest

There are no conflicts to declare.

Data availability

The data supporting this article have been included as part of the supplementary information (SI). Supplementary information: experimental details and spectral data. See DOI: https://doi.org/10.1039/d6ra01241h.

Acknowledgements

This work was supported by the National Natural Science Foundation of China (Grant No. 22301036). The authors extend their gratitude to Scientific Compass (https://www.shiyanjia.com) for BET analysis. AI-assisted tools were used solely for language polishing; all scientific content was generated by the authors.

Notes and references

1 A. Côté, A. Benin, N. Ockwig, M. O'Keeffe, A. Matzger and O. Yaghi, *Science*, 2005, **310**, 1166–1170.
2 K. Geng, T. He, R. Liu, S. Dalapati, K. Tan, Z. Li, S. Tao, Y. Gong, Q. Jiang and D. Jiang, *Chem. Rev.*, 2020, **120**, 8814–8933.
3 Y. Qian and H. Jiang, *Acc. Chem. Res.*, 2024, **57**, 1214–1226.
4 D. Jiang, V. Tan, Y. Gong, H. Shao, X. Mu, Z. Luo and S. He, *Chem. Rev.*, 2025, **125**, 6203–6308.
5 Y. Hu, S. Teat, W. Gong, Z. Zhou, Y. Jin, H. Chen, J. Wu, Y. Cui, T. Jiang, X. Cheng and W. Zhang, *Nat. Chem.*, 2021, **13**, 660–665.
6 L. Cusin, H. Peng, A. Ciesielski and P. Samorì, *Angew. Chem., Int. Ed.*, 2021, **60**, 14236–14250.
7 M. Lu, M. Zhang, C. Liu, J. Liu, L. Shang, M. Wang, J. Chang, S. Li and Y. Lan, *Angew. Chem., Int. Ed.*, 2021, **60**, 4864–4871.
8 C. Zhao, H. Lyu, Z. Ji, C. Zhu and O. Yaghi, *J. Am. Chem. Soc.*, 2020, **142**, 14450–14454.
9 S. Bi, F. Meng, D. Wu and F. Zhang, *J. Am. Chem. Soc.*, 2022, **144**, 3653–3659.
10 J. Liu, T. Yang, Z. Wang, P. Wang, J. Feng, S. Ding and W. Wang, *J. Am. Chem. Soc.*, 2020, **142**, 20956–20961.
11 X. Li, *Mater. Chem. Front.*, 2021, **5**, 2931–2949.
12 J. Segura, S. Royuela and M. Mar Ramos, *Chem. Soc. Rev.*, 2019, **48**, 3903–3945.
13 Q. Rong, X. Chen, Z. Huang, S. Li and S. He, *ACS Appl. Mater. Interfaces*, 2025, **17**, 3163–3171.
14 J. Wang, K. Song, T. Luan, K. Cheng, Q. Wang, Y. Wang, W. Yu, P. Li and Y. Zhao, *Nat. Commun.*, 2024, **15**, 1267.
15 X. Li, C. Zhang, S. Cai, X. Lei, V. Altoe, F. Hong, J. Urban, J. Ciston, E. Chan and Y. Liu, *Nat. Commun.*, 2018, **9**, 2998.
16 X. Li, J. Zou, T. Wang, H. Ma, G. Chen and Y. Dong, *J. Am. Chem. Soc.*, 2020, **142**, 6521–6526.
17 P. Das, J. Roeser and A. Thomas, *Angew. Chem., Int. Ed.*, 2023, **62**, e202304349.
18 R. Chen, C. Wu, L. Chung, J. Hu, M. Tang, Z. Lin, X. Yang, Z. Xu and J. He, *Chem. Mater.*, 2024, **36**, 9928–9938.
19 G. Jiang, W. Zou, Z. Ou, W. Zhang, J. Huo, S. Qi, L. Wang and L. Du, *Angew. Chem., Int. Ed.*, 2025, **64**, e202420333.
20 P. Das, G. Chakraborty, J. Roeser, S. Vogl, J. Rabeah and A. Thomas, *J. Am. Chem. Soc.*, 2023, **145**, 2975–2984.
21 K. Xie, G. Wang, F. Huang, F. Zhao, J. Kan, Z. Chen, L. Cai, S. Han, Y. Geng and Y. Dong, *Nat. Commun.*, 2025, **16**, 3493.
22 J. Hu, Z. Huang and Y. Liu, *Angew. Chem., Int. Ed.*, 2023, **62**, e202306999.
23 V. Martinez, T. Stolar, B. Karadeniz, I. Brekalo and K. Užarević, *Nat. Rev. Chem.*, 2022, **7**, 51–65.
24 C. Lennox, T. Borchers, L. Gonnet, C. Barrett, S. Koenig, K. Nagapudi and T. Friščić, *Chem. Sci.*, 2023, **14**, 7475–7481.
25 P. Baláž, M. Achimovičová, M. Baláž, P. Billik, Z. Cherkezova-Zheleva, J. M. Criado, F. Delogu, E. Dutková, E. Gaffet, F. J. Gotor, R. Kumar, I. Mitov, T. Rojac, M. Senna, A. Streletskii and K. Wieczorek-Ciurowa, *Chem. Soc. Rev.*, 2013, **42**, 7571.

26 D. Hasa and W. Jones, *Adv. Drug Delivery Rev.*, 2017, **117**, 147–161.
27 T. Friščić and W. Jones, *Cryst. Growth Des.*, 2009, **9**, 1621–1637.
28 A. Krusenbaum, S. Grätz, G. Tigineh, L. Borchardt and J. Kim, *Chem. Soc. Rev.*, 2022, **51**, 2873–2905.
29 A. Katsenis, A. Puškarić, V. Štrukil, C. Mottillo, P. Julien, K. Užarević, M. Pham, T. Do, S. Kimber, P. Lazić, O. Magdysyuk, R. Dinnebier, I. Halasz and T. Friščić, *Nat. Commun.*, 2015, **6**, 6662.
30 B. Biswal, S. Chandra, S. Kandambeth, B. Lukose, T. Heine and R. Banerjee, *J. Am. Chem. Soc.*, 2013, **135**, 5328–5331.
31 S. Emmerling, L. Germann, P. Julien, I. Moudrakovski, M. Etter, T. Friščić, R. Dinnebier and B. Lotsch, *Chem*, 2021, **7**, 1639–1652.
32 N. Brown, Z. Alsudairy, R. Behera, F. Akram, K. Chen, K. Smith-Petty, B. Motley, S. Williams, W. Huang, C. Ingram and X. Li, *Green Chem.*, 2023, **25**, 6287–6296.
33 E. Hamzehpoor, F. Effaty, T. Borchers, R. Stein, A. Wahrhaftig-Lewis, X. Ottenwaelder, T. Friščić and D. Perepichka, *Angew. Chem., Int. Ed.*, 2024, **63**, e202404539.
34 S. Hutsch, A. Leonard, S. Grätz, M. Höfler, T. Gutmann and L. Borchardt, *Angew. Chem., Int. Ed.*, 2024, **63**, e202403649.
35 H. Pan, N. Wang and G. Wang, *Chem. Commun.*, 2025, **61**, 8184–8187.
36 H. Pan, N. Wang and G. Wang, *Chem.–Eur. J.*, 2026, **32**, e70660.
37 J. Fu, L. Xie, J. Du, Z. Xu, Z. Shi, L. Hou and G. Li, *ACS Sustain. Chem. Eng.*, 2024, **12**, 13873–13884.
38 C. Wu, M. Shao, J. Kan, W. Liang, T. Li, L. Niu, H. Wang, Y. Geng and Y. Dong, *ACS Mater. Lett.*, 2024, **6**, 5016–5022.
39 R. Xue, Y. Liu, H. Guo, W. Yang and G. Yang, *J. Colloid Interface Sci.*, 2024, **655**, 709–716.
40 D. Y. Osadchii, A. I. Olivos-Suarez, A. V. Bavykina and J. Gascon, *Langmuir*, 2017, **33**, 14278–14285.
41 Y. Liang, M. Xia, Y. Zhao, D. Wang, Y. Li, Z. Sui, J. Xiao and Q. Chen, *J. Colloid Interface Sci.*, 2022, **608**, 652–661.
42 P. Das, G. Chakraborty, J. Yang, J. Roeser, H. Küçükkeçeci, A. Nguyen, M. Schwarze, J. Gabriel, C. Penschke, S. Du, V. Weigelt, I. Khalil, J. Schmidt, P. Saalfrank, M. Oschatz, J. Rabeah, R. Schomäcker, F. Emmerling and A. Thomas, *Adv. Energy Mater.*, 2025, 2501193.
43 Q. Rong, X. Chen, Q. Cheng, Z. Huang and S. He, *ACS Sustain. Chem. Eng.*, 2024, **12**, 13306–13315.
44 P. Das, G. Chakraborty, N. Friese, J. Roeser, C. Prinz, F. Emmerling, J. Schmidt and A. Thomas, *J. Am. Chem. Soc.*, 2024, **146**, 17131–17139.